Chapter 4

BIOLOGICALLY INSPIRED MICROROBOTICS

Islam S. M. Khalil* and Sarthak Misra†,‡

*The German University in Cairo, New Cairo City 11835, Egypt
†University of Twente, 7500 AE Enschede, The Netherlands
‡University of Groningen and University Medical Centre Groningen, Groningen 9700 RB, The Netherlands

The locomotion of microorganisms in low Reynolds number regimes has inspired engineers to design and fabricate robotic systems at micro- and nanoscales. Here, we review the swimming at low Reynolds number and analyze the kinematic reversibility property and the scallop theorem theoretically and experimentally. First, we present dynamical models for the planar flagellar and helical flagellar swimming of microorganisms. Second, we study the realization of microrobotic systems based on the mentioned locomotion mechanisms at micro- and nanoscales using fabrication based on nanotechnology. Finally, the locomotion mechanisms of the biologically inspired microrobotic systems are experimentally investigated using electromagnetic and magnetic systems.

1. The Journey to Biologically Inspired Microrobots

In seeking nutrients efficiently, microorganisms undergo different locomotion mechanisms. For example, peritrichously flagellated *Escherichia coli* swim by wrapping their flagella together in a helical bundle. The continuous rotation of this bundle enables locomotion and swimming back-and-forth. The *Escherichia coli* tumble whenever its necessary to change the swimming direction. Other monotrichous bacteria cannot tumble with a single flagellum. Therefore, they depend on rotational Brownian motion to change direction.[8] In his widely read lecture entitled *Life at Low Reynolds Number*,[9] Purcell explained the swimming strategies of microorganisms that are based on helical rotation without symmetry and more than one degree-of-freedom. Two opposite examples are again the *E. coli* and the scallop, the first rotate their flagellar bundle counterclockwise and the cells

rotate clockwise. This mechanism is based on more than one degree-of-freedom, whereas the scallop opens and closes its shell periodically and possesses one degree-of-freedom. The propulsion with helical rotation is not the only mechanism for locomotion. During their journey toward the ovum, sperm cells undergo a wide variety of swimming patterns by a beating their tail.[10] The sperm cell propagates in planar or 3D traveling wave (that breaks time-reversal symmetry) along the tail. This microorganism consists of a head and a flagellum that contains a mid-piece and an actively beating tail. The traveling waves are generated by local bending moment along the flagellum. This motion does not impart momentum to the fluid due to the absence of inertia, and hence, in the pursuit of locomotion at micro- and nanoscales, researches have mimicked and adapted swimming strategies of microorganisms.

Dreyfus *et al.* have mimicked the locomotion mechanism of the sperm cells by colloidal magnetic particles that are connected together using DNA and attached to a red blood cell.[1] The external magnetic fields have allowed this biologically inspired microrobot to be adjusted and driven using a flagellated swim (Fig. 1). Bell *et al.* have also fabricated artificial bacterial flagella and demonstrated the first locomotion mechanism based on the helical propulsion of the *E. coli*.[2] The artificial bacterial flagella is propelled using external rotating magnetic fields. In the same year (Fig. 1), Behkam *et al.* have demonstrated a novel hybrid micro-biorobot.[4] This microrobot is fabricated using polystyrene beads and driven by motile *Serratia marcescens* bacteria. The bacteria provide propulsive force to the bead that can be steered using external magnetic field. The coupling between the bead and the motile microorganism provides broad possibilities in biomedical application and nanotechnology. The microorganisms provide propulsive force to the bead without an onboard power source. In 2006, Martel *et al.* suggested that magnetotactic bacteria can be used as microrobots without coupling with another micro- or nanoobject.[16,19] Magnetotactic bacteria develop magnetite nanocrystals inside their cells, and hence their magnetic dipole moment enables directional control using external magnetic field. In addition, a swarm of magnetotactic bacteria have been used to achieve non-trivial tasks such as manipulation of spherical beads and microassembly of non-magnetic micro-objects.[20,21] We realize that in the pursuit of locomotion at low Reynolds number regime in micro- and nanoscales, scientists have either mimicked the designs of nature or used the microorganism itself to provide propulsion, as shown in Fig. 2. Behkam *et al.*[4] and Julius *et al.*[15] have used the same microorganisms, i.e. *S. marcescens*, to actuate beads and microbarge, respectively. In this case, bioadhesion has to be achieved between the motile cells and the surface of the bead or the micro-barge. Bioadhesion can be enhanced by the chemical treatment of these object to increase the attraction with the microorganisms. Another approach has been demonstrated by Magdanz *et al.* by achieving mechanical coupling between microtubes and

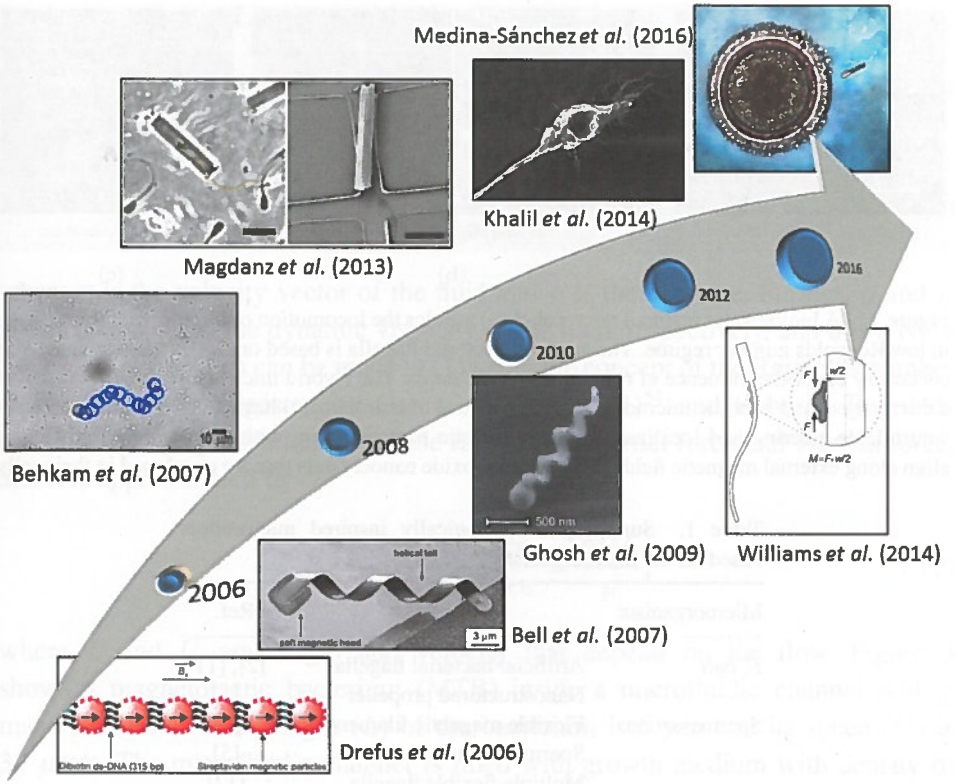

Figure 1. A time line of the development of biologically inspired microrobots. The first microrobot was developed by Drefus *et al.*[1] This microrobot breaks time-reversal symmetry using a propagating wave along its lumped structure. In 2007, Bell *et al.* fabricated and controlled the smallest artificial helical bacterial flagella using rotating magnetic fields,[2] and in 2009 Ghosh *et al.* decreased the size of the artificial bacterial flagella by 30 times in length.[3] Behkam *et al.*[4] and Magdanz *et al.*[5] presented the first hybrid micro-biorobots through coupling with *Serratia marcescens* bacteria (2007) and sperm cells (2013), respectively. In 2014, Khalil *et al.*[6] and Williams *et al.*[7] developed microrobots based on the propagation of planar waves through a flexible tail.

motile sperm cells (Fig. 2). The disadvantage of this approach is its low coupling efficiency due to the dependence on random coupling between sperm cells and the magnetic microtubes.[5,22] This coupling is necessary as the elements of the hybrid micro-biorobots are not useful alone, unlike magnetotactic bacteria that possess all elements required for locomotion and steering, i.e. flagellar propulsion and magnetic dipole moment.

Table 1 provides the contributions of some research groups in the field of biologically inspired microrobots. We primarily focus only on those designs that are or can be implemented at micro- and nanoscales. The work in this field has started in the last decade. Although other work has been proposed earlier, they were not at the micro- or nanoscale. For example, Honda *et al.* were the first

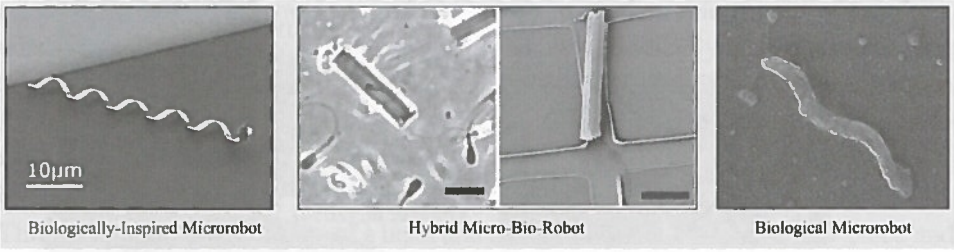

Figure 2. A biologically inspired microrobot (a) mimics the locomotion of microorganisms to swim in low Reynolds number regime. The artificial bacterial flagella is based on *E. coli*[2] and swims like a corkscrew under the influence of rotating magnetic fields. The Hybrid micro-biorobots (b) consist of a microobject and a motile microorganism. Biological microrobots (c) have all elements that enables controllable steering and localization. Magnetotactic bacteria swim with their helical flagella and align along external magnetic fields using the iron oxide nanocrystals that are enveloped in their cells.

Table 1. Summary of biologically inspired microrobots based on the microorganisms.

Microorganism	Microrobot	Ref.
E. coli	Artificial bacterial flagella	[2], [11]
	Nanostructured propeller	[3]
Spermatozoon	Flexible magnetic filament	[1]
	Sperm-in-a-tube	[5]
	Multiple flexible flagella	[12]
	Biohybrid swimmer	[7]
	MagnetoSperm	[6]
T. pyriformis	Magnetotactic *T. pyriformis*	[13]
	Magnetized *T. pyriformis*	[14]
S. marcescens	Bacteria-actuated microbarge	[15]
	Bacteria-driven beads	[4]
MTBs	Swarm of bacteria	[16]
	Single bacterium	[17], [18]

group to demonstrate helical propulsion on macroscale in 1996.[23] Their design achieves locomotion by imparting momentum to the fluid. In this chapter, we study the microrobotic systems that cannot impart momentum to the fluid but rather utilize and adopt different strategies to navigate at low Reynolds number. The remainder of this chapter is organized as follows: Section 2 provides descriptions pertaining to locomotion at low Reynolds number through breaking time-reversal symmetry using planar and helical propulsion. A facile fabrication technique (based on electrospinning) to provide robotic sperms is presented in Sec. 3. An overview of the motion control of biologically inspired microrobotic system using magnetic-systems with closed- and open-configuration is included in Sec. 4. Finally, Sec. 5 concludes and provides directions for future studies.

2. Locomotion at Low Reynolds Number

Dynamics of all fluids is governed by Navier–Stokes equations that consists of the following Newtons second law and the continuity equation[25]:

$$\frac{\partial \mathbf{u}}{\partial t} + \mathbf{u} \cdot \nabla \mathbf{u} = -\frac{1}{\rho}\nabla p + \frac{\mu}{\rho}\nabla^2 \mathbf{u} + \mathbf{b} \quad \text{and} \quad \nabla \cdot \mathbf{u} = 0, \tag{1}$$

where $\mathbf{u}$ is the velocity vector of the fluid and p is the pressure. Further, ρ and μ are the density and the dynamic viscosity of the fluid, respectively, and $\mathbf{b}$ is a body force. Simplifications can be made to (1) using the concept of the Reynolds number which has been suggested by Gabriel Stokes (1851)[54] and Osborne Reynolds (1883).[55] The Reynolds number is the ratio of the inertial force and viscous force, and it is approximated by

$$R_e \triangleq \frac{\text{Inertial force}}{\text{Viscous force}} = \frac{\rho U L}{\mu}, \tag{2}$$

where L and U are length and velocity that depend on the flow. Figure 3 shows a magnetotactic bacterium (MTB) inside a microfluidic channel with a maze structure.[24] The length (L) of the bacterium is 5 μm and its speed (U) is 35 μm/s. The microfluidic channel is filled with growth medium with density of approximately 1000 kg/m^3 and dynamic viscosity (μ) of 10^{-3} Pa·s. Therefore, Reynolds number is on the order of 1.75×10^{-4}. Reynolds number has another interpretation, let us assume that we control the flow of the growth medium of the

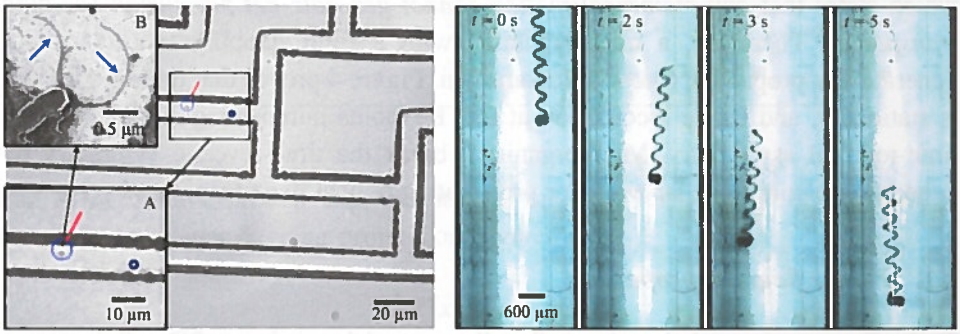

(a) (b)

Figure 3. Helical flagellated swim is achieved by magnetotactic bacteria (*Magnetospirillum magnetotacticum* Strain MS-1) and helical microrobots inside a microfluidic chip with maze structure[24] and a catheter segment, respectively. (a) The magnetotactic bacterium is controlled by directing the magnetic fields and swim using its flagella. (b) The helical microrobot is propelled using rotating magnetic fields.

MTB inside the microfluidic channel. In this case, L is the width of the channel and U is the flow of the growth medium, and hence Reynolds number has different interpretations that depend on the flow situation. Another example is the helical microrobots in Fig. 3; it swims using helical propulsion under the influence of external rotating magnetic fields inside a catheter segment with controlled flow. The Reynolds number of this microrobot is on the order of 1.3. Inducing a flow in the catheter segment would enable another interpretation of Reynolds number, where the flow and inner diameter of the segment are represented using U and L, respectively. In contrast to the propulsion of the helical microrobot that relays on imparting momentum to the fluid ($R_e = 1.3$), an MTB depends solely on viscous damping ($R_e = 1.75 \times 10^{-4}$). Therefore, we can ignore the inertial terms in (1) and make some simplifications to obtain the following linear Stokes equation:

$$\nabla p = \mu \nabla^2 \mathbf{u} \quad \text{and} \quad \nabla \cdot \mathbf{u} = 0. \tag{3}$$

We observe the following properties from Stokes equation:

1. Stokes equations are linear, unlike Navier–Stokes equation (1);
2. In contrast to Navier–Stokes equations, Stokes equations are time-reversible;
3. The instantaneous structure of the flow does not depend on the history of motion, but rather on the present configuration.

The second property is illustrated experimentally in Fig. 4. Three paramagnetic microparticles are attached together and oscillate under the influence of weak oscillating magnetic field (**B**). The magnetic fields are uniform and do not exert magnetic force on the dipole moment (**m**) of the microparticles. This reciprocal (flapping) motion cannot generate any propulsion due to absence of inertia. The experiment provided in Fig. 4 is nothing but the scallop theorem of Purcell which states that *any reciprocal motion cannot generate net propulsion (or fluid transport)*.[9] Therefore, a microorganism with a rigid flapping motion cannot generate any propulsive force for locomotion. Figure 4 proves that the rigid flapper is stationary, and hence locomotion at low Reynolds number regime necessitates time-reversal asymmetry. Microorganisms break the time-reversal symmetry by generating planar flagellar waves or propagating helical flagellar waves.

2.1. *Planar flagellar propulsion*

Taylor[26] approximated the planar flagellar propulsion using a 2D infinite wave $\Psi(x, y, t)$ in a velocity fields, $\mathbf{v} = u\hat{\mathbf{x}} + v\hat{\mathbf{y}}$. A propulsion speed ($U$) develops for a traveling wave along the opposite direction. The elements of the velocity field are given by

$$u = \frac{\partial \Psi}{\partial y}(x, y, t) \quad \text{and} \quad v = -\frac{\partial \Psi}{\partial x}(x, y, t). \tag{4}$$

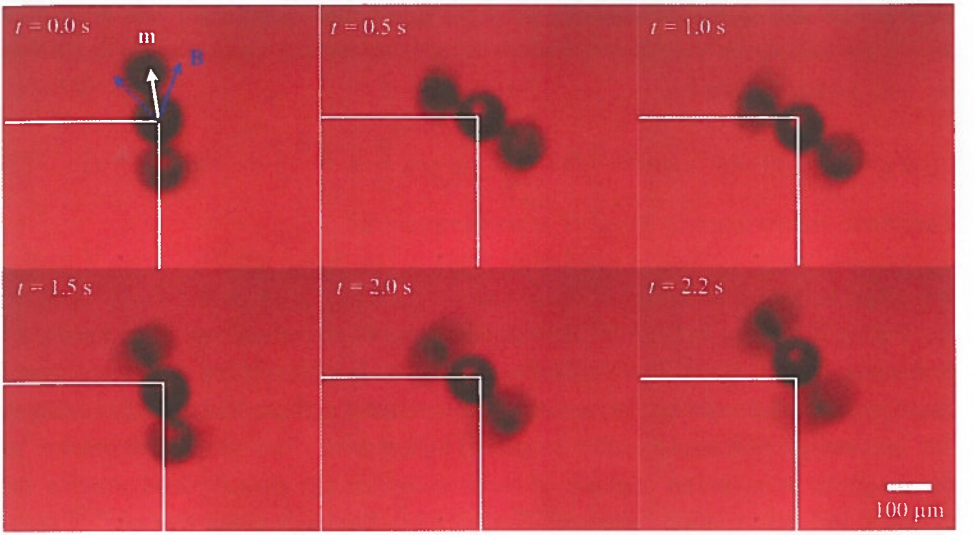

Figure 4. A cluster of three paramagnetic microparticles undergoes a rigid flapping under the influence of oscillating magnetic fields. This rigid reciprocal motion does not provide propulsion at low Reynolds number. Therefore, the cluster is almost stationary in all time instants. The arrow along the long axis of the cluster represents its magnetic dipole moment, whereas the other arrows indicate the periodic magnetic field. The white lines indicate the initial position of the cluster.

Table 2. Boundary conditions of the biharmonic equation.

First order	BCs	Second order	BCs
$\frac{\partial \Psi_1}{\partial y}\|_{x,y\longmapsto\infty}$	U_1	$\frac{\partial \Psi_2}{\partial y}\|_{x,y\longmapsto\infty}$	U_2
$\frac{\partial \Psi_1}{\partial x}\|_{x,y\longmapsto\infty}$	0	$\frac{\partial \Psi_2}{\partial x}\|_{x,y\longmapsto\infty}$	0
$\frac{\partial \Psi_1}{\partial y}\|_{x,y=0}$	0	$\frac{\partial \Psi_2}{\partial y}\|_{x,y=0}$	$-\sin(x-t)\frac{\partial^2 \Psi_1}{\partial y^2}\|_{x,y=0}$
$\frac{\partial \Psi_1}{\partial x}\|_{x,y=0}$	$\cos(x-t)$	$\frac{\partial \Psi_2}{\partial x}\|_{x,y=0}$	$-\sin(x-t)\frac{\partial^2 \Psi_1}{\partial y \partial x}\|_{x,y=0}$

Pak *et al.*[25] have proven that the stream function formulation of the Stokes equations for planar flagellar propulsion is given by

$$\nabla^4 \Psi(x, y, t) = 0. \tag{5}$$

It has been also shown that (when the wave amplitude is much smaller than the wavelength) solution of (5) with the boundary condition in Table 2 is approximated by

$$\psi = \varepsilon \psi_1 + \varepsilon^2 \psi_2 + \cdots \quad \text{and} \quad U = \varepsilon U_1 + \varepsilon^2 U_2 + \cdots, \tag{6}$$

where $\varepsilon = ak$ is the dimensionless wave amplitude. Further, a and k are the amplitude and wave number, respectively. The first- and second-order solutions (ψ_1 and ψ_2) are given by

$$\psi_1 = (1+y)\exp^{-y}\sin(x-t) \quad \text{and} \quad \psi_2 = \frac{y}{2} - \frac{y\exp^{-2y}}{2}\cos 2(x-t). \tag{7}$$

Therefore, the swimming speed U is proportional to

$$U \sim a^2k^2c. \tag{8}$$

Figure 5 shows a flexible flapping motion of a sperm-shaped microrobot[27] at frequency of 1 Hz.[28] The flexibility of the tail enables wave propagation and breaking of the time-reversal symmetry. We construct a numerical model to analyze the motion of this biologically inspired microrobot. The numerical model of the magnetic microrobot consists of three components: elastohydrodynamics for dynamic tail deformation based on Timoshenko–Rayleigh beam theory,[29,30] magnetohydrodynamics based on the Biot–Savart law for electromagnetic coils,[31,32] and rigid-body kinematics based on transient Stokes-flow approach with force-free swimming conditions.[26,33] Each component utilizes resistive force coefficients based on resistive-force theory[8,34] to calculate the resultant hydrodynamic forces

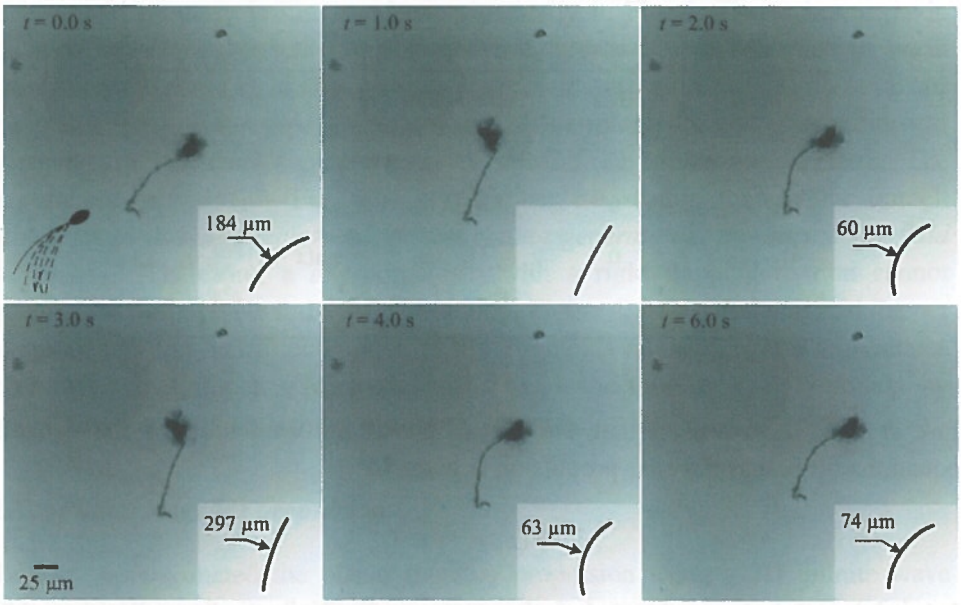

Figure 5. Flexibility of the tail of the sperm-shaped microrobot is demonstrated under the influence of oscillating magnetic field at 1 Hz. This flexibility enables a non-reciprocal deformation and flagellated swim. The radius of curvature is provided at each time instant, and the tail is almost straight at time $t = 1.0$ s. The tail deformations are overlaid and schematically represented in the bottom-left corner of the first time instant.

acting on the elastic tail and magnetic body of the swimmer. The equation of motion of the magnetic microrobot based on the force-free swimming condition[8] is given by

$$\begin{bmatrix} \mathbf{V} \\ \boldsymbol{\Omega} \end{bmatrix} = -\mathbf{B}_{sw}^{-1} \begin{bmatrix} \mathbf{F}_{mag} + \mathbf{F}_{add} \\ \mathbf{T}_{mag} + \mathbf{T}_{add} \end{bmatrix}, \tag{9}$$

where $\mathbf{V}$ and $\boldsymbol{\Omega}$ are the linear and angular rigid-body velocities of the microrobot, respectively. Further, $\mathbf{F}_{mag}$ and $\mathbf{F}_{add}$ are the magnetic force and inertial force due to added mass on the microrobot, respectively. Further, $\mathbf{T}_{mag}$ and $\mathbf{T}_{add}$ are the magnetic torque and the inertial torque due to added mass acting on the microrobot, respectively. In addition, $\mathbf{B}_{sw}$ is the resistance matrix of the microrobot that consists of the resistance matrices of the body ($\mathbf{B}_b$) and the tail ($\mathbf{B}_t$), and it is given by

$$\mathbf{B}_{sw} = \mathbf{B}_b + \mathbf{B}_t. \tag{10}$$

In (10), the resistance matrix of the body is represented using

$$\mathbf{B}_b = \begin{bmatrix} \mathbf{D}_{tran} & -\mathbf{D}_{tran}\mathbf{S}_b \\ \mathbf{S}_b\mathbf{D}_{tran} & \mathbf{D}_{rot} \end{bmatrix}, \tag{11}$$

where $\mathbf{D}_{tran}$ and $\mathbf{D}_{rot}$ are the diagonal matrices of translational and rotational resistive force coefficients of the body, and $\mathbf{S}_b$ is a skew-symmetric matrix signifying the cross-products. In (10), $\mathbf{B}_t$ is given by

$$\mathbf{B}_t = \int_0^{l_t} \begin{bmatrix} \mathbf{RCR}^T & -\mathbf{RCR}^T\mathbf{S}_t \\ \mathbf{S}_t\mathbf{RCR}^T & -\mathbf{S}_t\mathbf{RCR}^T\mathbf{S}_t \end{bmatrix} \mathrm{d}l, \tag{12}$$

where l_t is the length of the sperm-shaped microrobot. Further, $\mathbf{C}$ and $\mathbf{R}$ are the diagonal matrix of the local resistive force coefficients, and the rotation matrix from local Frenet–Serret coordinate frames to the inertial frame of the reference of the microrobot along the elastic tail, respectively. Furthermore, $\mathbf{S}_t$ is another skew-symmetric matrix signifying the cross-products. The magnetic force ($\mathbf{F}_{mag}$) and torque ($\mathbf{T}_{mag}$) acting on the magnetic body are given by

$$\begin{bmatrix} \mathbf{F}_{mag} \\ \mathbf{T}_{mag} \end{bmatrix} = \begin{bmatrix} \mathbf{R}_{sw}^T V (\mathbf{M} \cdot \nabla) \mathbf{B} \\ V\mathbf{M} \times \mathbf{B} \end{bmatrix}, \tag{13}$$

where V is the volume of the magnetic material and $\mathbf{M}$ is its magnetization in the frame of the laboratory. Further, $\mathbf{B}$ is the magnetic flux density vector. The frame of the electromagnetic system and the frame of the microrobot are related using the rotation matrix ($\mathbf{R}_{sw}$). The components of the electromagnetic fields generated

using our electromagnetic configuration are calculated using[35]

$$B_x = \left(\frac{5}{4}\right)^{\frac{3}{2}} \frac{B_0}{4\pi} \int_0^{2\pi} \left(1 - \frac{y}{r}\cos\theta - \frac{z}{r}\sin\theta\right) F_0^{\frac{3}{2}} \mathrm{d}\theta, \tag{14}$$

where B_x is the magnetic field along x-axis and r_i is the inner radius of the electromagnetic coil. B_0 is given by

$$B_0 = \left(\frac{5}{4}\right)^{\frac{3}{2}} \frac{\mu_0 N I_c}{r}. \tag{15}$$

In (15), μ_0, N, and I_c are the permeability of the iron core, number of turns of each coil, and the input current on each of the electromagnetic coils, respectively. Further, F_0 is given by

$$F_0 = \left(\frac{x}{r}\right)^2 + \left(\frac{y}{r} - \cos\theta\right)^2 + \left(\frac{z}{r} - \sin\theta\right)^2, \tag{16}$$

The magnetic field along y-axis is given by

$$B_y = \left(\frac{5}{4}\right)^{\frac{3}{2}} \frac{B_0}{4\pi} \int_0^{2\pi} \left(\frac{x}{r} \frac{\cos\theta}{F_0^{\frac{3}{2}}}\right) \mathrm{d}\theta, \tag{17}$$

furthermore, the magnetic field along z-axis is given by

$$B_z = \left(\frac{5}{4}\right)^{\frac{3}{2}} \frac{B_0}{4\pi} \int_0^{2\pi} \left(\frac{x}{r} \frac{\sin\theta}{F_0^{\frac{3}{2}}}\right) \mathrm{d}\theta. \tag{18}$$

The magnetic field gradient can also be calculated using (15), (17), and (18) to determine the magnetic force (13) exerted on the magnetic dipole of the microrobot. The structural deformation in the frame of the microrobot is calculated based on the Timoshenko–Rayleigh beam model,[29,30] in order to take the vibration effect and large deformations into account for high actuation frequencies and axial shear forces. Finally, the transient hydrodynamic force due to the added mass is calculated using[17]

$$\begin{bmatrix} \mathbf{F}_{\text{add}} \\ \mathbf{T}_{\text{add}} \end{bmatrix} = \begin{bmatrix} \Phi \int_{-\infty}^{t} \frac{\mathrm{d}\mathbf{V}}{\mathrm{d}t} \frac{\mathrm{d}\tau}{\sqrt{t-\tau}} - \frac{2}{3}\pi R^3 \rho_l \frac{\mathrm{d}\mathbf{V}}{\mathrm{d}t} \\ \mathbf{S}_b \mathbf{F}_{\text{add}} \end{bmatrix}, \tag{19}$$

where ρ_l is the density of the liquid medium and R is the radius of the body. In (13), Φ is calculated as $\Phi = 6R^2\sqrt{\pi\mu\rho_l}$, where μ is the dynamic viscosity of the liquid environment. The driving currents on the coils are modeled as:

$$i_A = i_C = I_{\max} \sin\left(\Omega_z + \frac{\pi}{4}\cos(2\pi f t)\right), \tag{20}$$

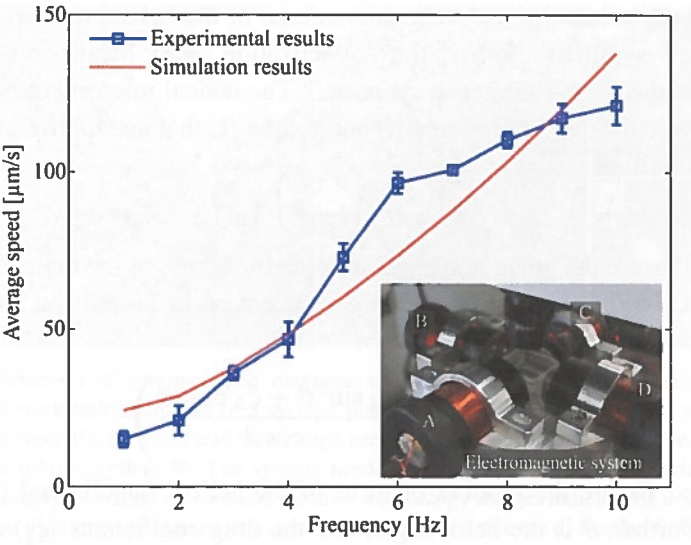

Figure 6. Experimental and simulation frequency response of sperm-shaped microrobots. The average speed is calculated from 10 trials for each frequency.[28] The maximum swimming speed is observed at frequency of 10 Hz. The simulation results are calculated using 9. The diameter of the head is 40 μm, and the length of the tail is 100 μm. Oscillating magnetic fields are generated by applying the currents inputs (20) and (21) to the four electromagnetic coils.

where i_A and i_C are the current inputs to electromagnetic coils A and C (Fig. 6), respectively. Further, I_{max} and f are the maximum input current and the frequency, respectively. The current inputs to electromagnetic coils B(i_B) and D(i_B) are given by

$$i_B = i_D = I_{max} \cos\left(\Omega_z + \frac{\pi}{4}\cos(2\pi f t)\right). \tag{21}$$

Our model is verified by comparing its results to the experimental frequency response of the microrobot, as shown in Fig. 6. The swimming speed of the sperm-shaped microrobot increases almost linearly with the frequency of the oscillating fields. This frequency response experiment is achieved using an electromagnetic system with orthogonal configuration, and currents (20) and (21) are supplied to the electromagnetic coils.

2.2. *Helical flagellar propulsion*

A helical microrobot is subjected to the following magnetic force (**F**) and magnetic torque (**T**) under the influence of external magnetic fields:

$$\begin{pmatrix}\mathbf{F}\\ \mathbf{T}\end{pmatrix} = V\begin{pmatrix}(\mathbf{M}\cdot\nabla)\mathbf{B}\\ (\mathbf{M}\times\mathbf{B})\end{pmatrix} = V\begin{pmatrix}(\mathbf{M}\cdot\nabla)\mathbf{B}\\ \hat{\mathbf{M}}\mathbf{B}\end{pmatrix}, \tag{22}$$

where V is the volume of the magnetic material of the helical microrobot. In (22), $\hat{\mathbf{M}}$ is the skew-symmetric form of the magnetization vector $\mathbf{M}$, where $\hat{\mathbf{M}} = \mathrm{SK}(\mathbf{M})$, and $\mathrm{SK}(\cdot)$ is the skew-symmetric operator.[36] The helical microrobot navigates in a viscous flow and experiences force ($\mathbf{f}$) and torque ($\mathbf{t}$) that are approximated by[37]

$$\begin{pmatrix} \mathbf{f} \\ \mathbf{t} \end{pmatrix} = -\begin{pmatrix} a & b \\ b & c \end{pmatrix} \begin{pmatrix} \mathbf{v} \\ \omega \end{pmatrix}, \tag{23}$$

where $\mathbf{v}$ and ω are the linear and angular velocity vectors of the helical microrobot, respectively. Further a, b, and c are the coefficient of the propulsion matrix and are given by

$$a = 2\pi n R_h \left(\frac{\xi_{\parallel} \sin^2\theta + \xi_{\perp} \cos^2\theta}{\cos\theta} \right), \tag{24}$$

where n and R_h are the number of turns of the helical flagella and the radius of the helix. Further, θ is the helix angle, and the drag coefficients ($\xi_{\parallel}$) and ($\xi_{\perp}$) are given by

$$\xi_{\parallel} = \frac{4\pi\eta a}{\ln\left(\frac{2a}{b}\right) - \frac{1}{2}} \quad \text{and} \quad \xi_{\perp} = \frac{8\pi\eta a}{\ln\left(\frac{2a}{b}\right) + \frac{1}{2}}, \tag{25}$$

where a and b are the major and minor diameter of the elliptical head of the helical microrobot, and η is the dynamic viscosity of the medium. In (25), b is given by

$$b = 2\pi n R_h^2 \left(\xi_{\parallel} - \xi_{\perp}\right) \sin\theta. \tag{26}$$

Finally, c is calculated using

$$c = 2\pi n R_h^3 \left(\frac{\xi_{\parallel} \cos^2\theta + \xi_{\perp} \sin^2\theta}{\cos\theta} \right). \tag{27}$$

The motion of the helical microrobot is governed by (22) and (23).

3. Synthetic Biologically Inspired Microrobots

The advancements in nanotechnology enable fabrication of biologically inspired microrobots at the nano- and microscales. We focus on the fabrication of sperm-shaped microrobots, and readers are referred to the original papers of Bell *et al.*[2] and Fischer *et al.*[3] for details on the fabrication of helical microrobots. The sperm-shaped microrobots are fabricated by electrospinning[38,39] using a solution, i.e. polystyrene and dimethylformamide, that is slowly injected through a needle via a syringe pump ①. This solution is mixed with iron oxide nanoparticles. An electrical potential is applied using a high voltage power supply ⑥ between the needle ② and the collector ③ to introduce free charge at the liquid surface (Fig. 7(a)). The free charge generates electric stress that causes the liquid jet to stretch into fine filaments

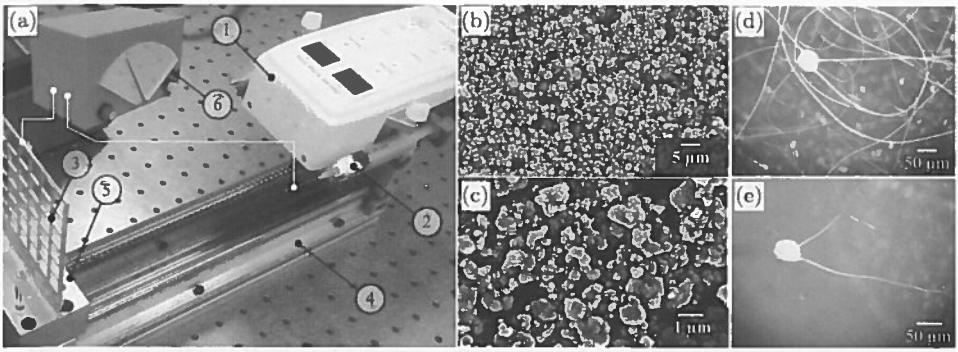

Figure 7. Fabrication of sperm-shaped magnetic microrobots using electrospinning.[28] (a) The electrospinning workstation consists of a syringe pump ①, a syringe needle ②, and a collector ③. The distance between the collector and the syringe needle is controlled using a linear motion stage ④ and a cartesian robotic system ⑤. The syringe needle and the collector are connected to a high-voltage power supply ⑥. (b and c) Scanning electron microscopy images indicate the iron oxide nanoparticles that are used to provide magnetic dipole moment to the fibers. (d) Beaded fibers are formed when electric potential is increased to a few kilovolts. (e) The sperm-shaped microrobots are cut and separated from the fibers. The magnetic head provides directional control under the influence of the external magnetic fields, whereas the flexible tail provides propulsive force using flagellated swim.

and accelerate away from the needle toward the collector. The liquid meniscus at the needle opening forms a conical shape when the electrical potential is increased to 10 kV. A liquid jet with high charge density is observed at the cone apex where the free charge is highly concentrated. On the way from the needle to the collector, the liquid jet stretches via bending instability, and hence increases its surface area. Furthermore, the solvent of the polymer solution evaporates until the jet solidifies and the beaded fibers are localized on the collector. Rayleigh instability occurs if the diameter of the jet is relatively small and if the solution is in liquid state. This instability allows the jet to disintegrate into beads. If the jet is very thin and the solvent is evaporated, the Rayleigh instability is suppressed.[38]

The transition from formation of beads, beads with fibers, and pure fibers depends on increasing the initial concentration of the polymer.[38] Beaded fibers (Fig. 7(b)) are formed on the collector for solutions with intermediate viscosity. We extract the beaded fibers from the metallic grit collector ③. Then, the collected structures are cut and extracted using tweezers under high magnification. One cut is made close to the bead, and the second is made based on the desired length of the tail (l_t). This procedure leads to a geometry that resembles the morphology of a sperm cell, as shown in Figs. 7(e) and 8. The beads provide the magnetic dipole, whereas the propulsive force is generated by the ultra-thin fiber using a flagellated swim. Motion of the sperm-shaped microrobot is controlled using an electromagnetic system with orthogonal configuration (Fig. 6).

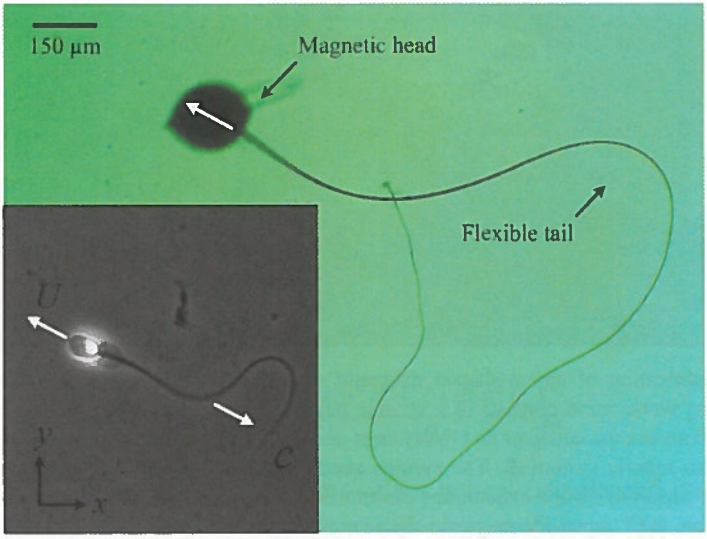

Figure 8. A sperm-shaped microrobot fabricated using electrospinning that resembles the morphology of a sperm cell (inset).[28] This microrobot consists of a microbead and an ultra-fine fiber, morphologically similar to a sperm cell. The microbead contains iron oxide nanoparticles and provides magnetization (**M**), whereas the fiber provides propulsive force when oscillating magnetic fields are applied.

4. Magnetic Control and Applications

In contrast to microrobotic system that are powered and steered using bubble propulsion,[40] electric propulsion,[41] ultrasound-propulsion,[42] and self-electrophoretic propulsion, the majority of the biologically inspired microrobots are propelled and steered using external source of magnetic fields. These fields are generated using electromagnetic and magnetic systems with closed configurations[43] and open configurations,[44] as shown in Fig. 9. The function of these configurations of electromagnetic coils is twofold: first, to provide magnetic field lines that direct the microrobot (the easy axis of the microrobot[45]) toward a reference position; second, to rotate or oscillate these fields to enable propulsion. The embedded magnetic layer permits the microrobot to align along these fields, and hence rotate or oscillate to provide helical propulsion of planar wave, respectively. Let us analyze the dynamics of a helical microrobot in a controlled magnetic field. A simple motion control strategy is based on directing the magnetic field lines toward a reference position. Therefore, we use the rotational dynamics of the helical microrobot to analyze and design the control input. Using (22) and (23), we obtain the following rotational dynamics of the helical microrobot:

$$V\hat{\mathbf{M}}\mathbf{B} - b\mathbf{v} - c\boldsymbol{\omega} = 0. \tag{28}$$

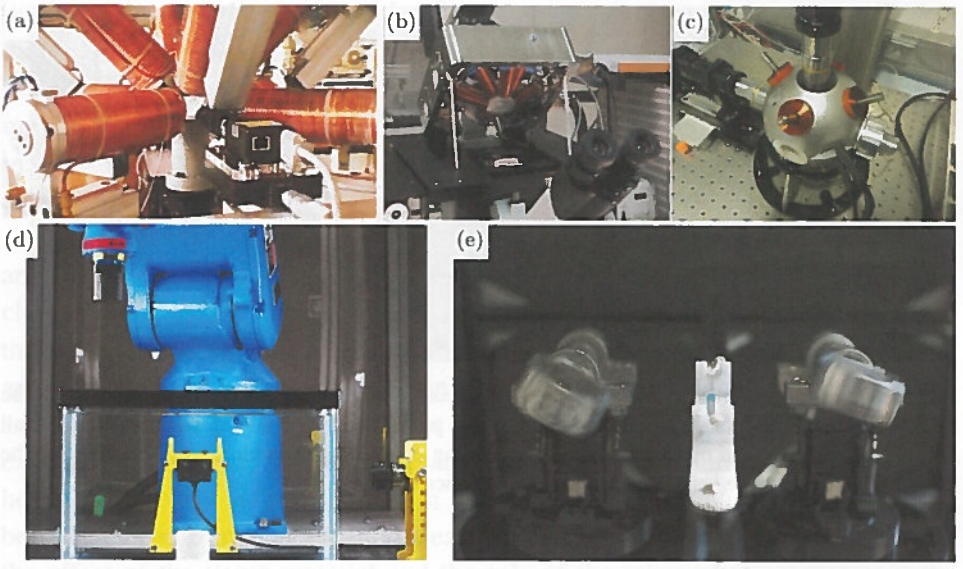

Figure 9. Electromagnetic and magnetic systems for the control microrobotic systems. (a) The OctoMag configuration is an electromagnetic system that enables motion control of microrobots in 3D space.[36] (b) The MiniMag configuration also allows for control in 3D space.[43] (c) An electromagnetic system enables 3D control along with automatic focusing.[46] (d) Magnetic system with open configuration for the control of magnetically actuated tools.[47] (e) Magnetic system with two rotating dipole fields.[48]

The magnetic field ($\mathbf{B}$) is controlled to align the microrobot (let us assume simple rotations) toward a reference position. Therefore, the angular position and velocity errors ($\mathbf{e}$ and $\dot{\mathbf{e}}$) are given by

$$\mathbf{e} = \Phi - \Phi_{\text{ref}} \quad \text{and} \quad \dot{\mathbf{e}} = \dot{\Phi} = \omega, \tag{29}$$

where Φ and Φ_{ref} are the angular position of the microrobot and the fixed reference orientation that directs the microrobot towards the reference position, respectively. We rewrite (28) using (29), and devise a proportional control input ($\mathbf{B} \mapsto \mathbf{K}_{\text{p}}\mathbf{e}$) to obtain the following error dynamics:

$$\dot{\mathbf{e}} - \frac{V}{c}\hat{\mathbf{M}}\mathbf{K}_{\text{p}}\mathbf{e} = -\frac{b}{c}\mathbf{v}. \tag{30}$$

We select the following storage function $S(\mathbf{e})$:

$$S(\mathbf{e}) = \frac{1}{2}\mathbf{e}^{\text{T}}\mathbf{e}. \tag{31}$$

Taking the time-derivative of (31) yields

$$\dot{S}(\mathbf{e}) = \frac{V}{c}\mathbf{e}^{\text{T}}\mathbf{K}_{\text{p}}^{\text{T}}\hat{\mathbf{M}}^{\text{T}}\mathbf{e} - \frac{b}{c}\mathbf{v}^{\text{T}}\mathbf{e} \leq -\mathbf{v}^{\text{T}}\mathbf{e}. \tag{32}$$

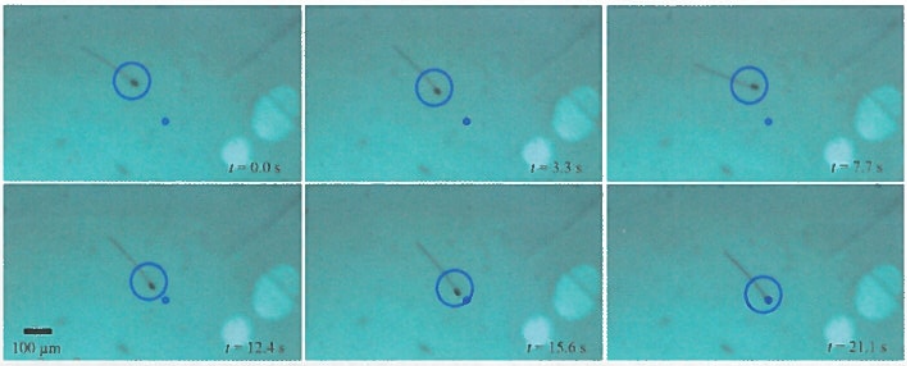

Figure 10. A representative closed-loop motion control of the sperm-shaped microrobot. The sperm-shaped microrobot slides on the bottom of the petri dish toward the reference position (small circle) at a sliding speed of 12 μm/s, at an oscillating magnetic field with frequency of 5 Hz. The large circle indicates the head of the sperm-shaped microrobot.

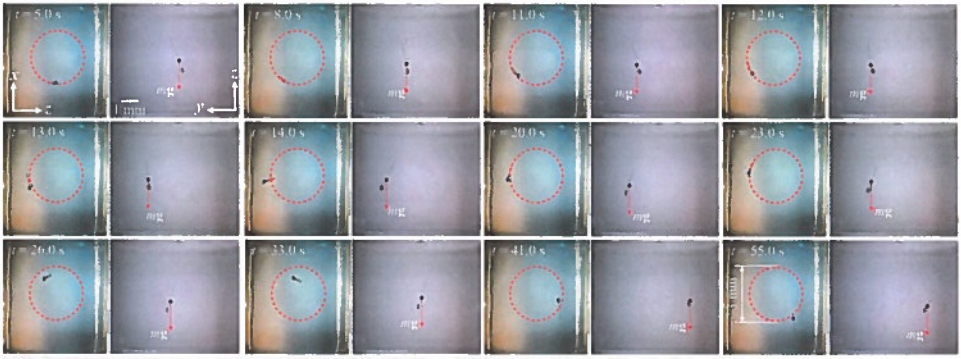

Figure 11. The helical microrobot is following a circular trajectory in xz-plane with a diameter of 3 mm. The force ($m\mathbf{g}$) due to gravity is compensated by the helical propulsion of the microrobot (yz-plane), where m is the mass of the microrobot and $\mathbf{g}$ is the acceleration due to gravity. The speed of the microrobot is calculated to be 171 μm/s, at a frequency of 8 Hz.

Therefore, the system with the input $(-\mathbf{v})$ and output $(\mathbf{e})$ is passive with the storage function $(S(\mathbf{e}))$. This control strategy enables directional control of the microrobot toward the reference position. The oscillation or rotation of these fields allows for propulsion along these field lines as shown in Figs. 10 and 11. The oscillating field enables the sperm-shaped microrobot to orient toward a reference position (small circle) and achieve a flagellated swim under the influence of oscillating field of 5 Hz, as shown in Fig. 10. A helical propulsion is also achieved using the same control strategy in 3D space using a helical microrobot, as shown in Fig. 11. The helical microrobot follows a circle (dashed circle) along xz-plane and overcomes

its weight by providing a propulsive force component along z-axis. An oscillating magnetic field of 8 Hz enables helical flagellated swim at a speed of 171 μm/s.

The control result shown in this chapter indicates that biologically inspired microrobots hold promise in medical and diverse nanotechnology applications. For instance, the helical microrobots can be coated with a chemotherapeutic agent and controlled toward a diseased region to achieve targeted therapy. Helical microrobots also have the potential to be used in clearing of clogged blood vessels or the arterial plaque.[49] Figure 12 shows a helical microrobot drilling through a blood clot inside a catheter segment under the influence of rotating magnetic fields. In this experiment, the helical microrobot decreases the size of the blood clot by approximately 50% following 36 min of drilling using magnetic field of 20 mT and frequency of 6 Hz.[50] Mahoney *et al.*[51] have experimentally demonstrated the existence of magnetic torques that can simultaneously stabilize and destabilize a helical microrobot in soft tissue. An empirical model of helical microrobot has been developed from experimental measurements in an agar gel phantom to predict the effect of the tissue material and the role of the microrobot geometry on the resulting trajectory.[52] Despite this progress in fabrication, actuation, and control of helical microrobots, numerous challenges remain for translating these microrobots into *in vivo* applications such as the following: first, the flow rates of blood in aorta, arteries, capillaries, veins, and vena cava are higher than the flow rates used in this study and necessitate larger magnetic field gradient to move and hold the microparticles against the flow of bodily fluids; second, a clinical imaging modality

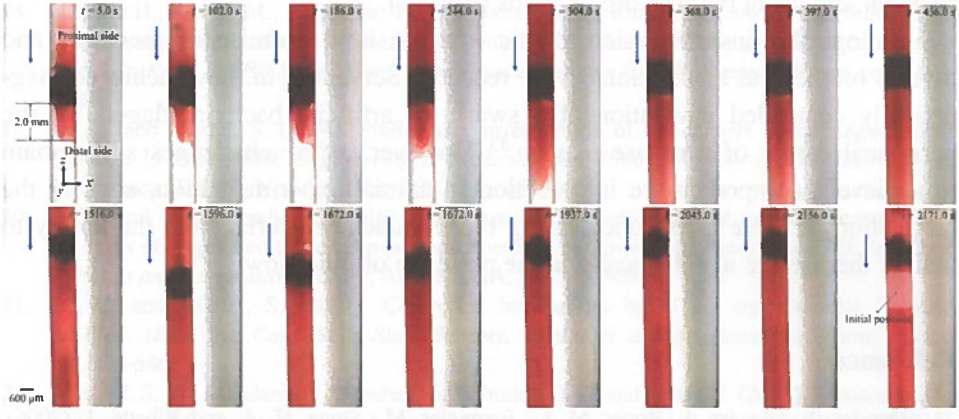

Figure 12. Penetration of a blood clot with diameter and width of 3 mm and 5 mm, respectively, is achieved using a helical microrobot.[50] The microrobot swims in the phosphate buffered saline at an average speed of 600 μm/s, and contact with the blood clot is observed at time $t = 5$ s. At time $t = 436$ s, the blood clot becomes mobile, and both rotation and translation along the catheter segment are observed. In this representative experiment, the size of the blood clot is decreased by 50% following 36 minutes of drilling using the microrobot.

must be integrated with the electromagnetic configuration to provide feedback to the control system, and its resolution has to be at the microscale; and third, the biocompabitability and physiological conditions of the drug release must be studied and implemented experimentally.

5. Concluding Remarks

In this chapter, we have studied two propulsion mechanisms of microorganisms that are used in the design and implementation of microrobotic systems. We have focused on the modeling, fabrication, and motion control using external magnetic fields. We have provided a proof-of-concept experiment for a rigid reciprocal swimmer (Fig. 4) in low Reynolds number regime and demonstrated that propulsion cannot be achieved as this swimmer does not impart momentum in the medium. We have also shown a fabrication technique (Fig. 7) to develop microrobots with a similar morphology to sperm cells. The flexibility of the artificial flagellum of the sperm-shaped microrobot enables wave propagation (Fig. 5) and breaking of the time-reversal symmetry. The motion of this microrobot is modeled using elastohydrodynamics approach and Timoshenko–Rayleigh beam theory, and we find agreement with the frequency response experimental results. This chapter also provides a general control strategy to orient the microrobots toward a desired direction. This strategy is tested on a helical microrobot and a sperm-shaped microrobot and enables motion in 3D and 2D spaces. We have also showed the helical microrobots can be used to clear blood clots *in vitro* inside a catheter segment and using rotating dipole fields (Fig. 12).

Biologically inspired microrobotic systems hold promise in medicine and diverse biomedical applications. Very recently, Servant *et al.* have achieved magnetically controlled navigation of a swarm of artificial bacterial flagella in the peritoneal cavity of a mouse *in vivo*.[53] However, a few challenges still remain to achieve a comprehensive intervention in animal experimentation, such as the fabrication of these microrobots using biodegradable materials and the ability to deliver therapeutic agents locally in the presence of fluid flow.

References

1. Dreyfus, R., Baudry, J., Roper, M. L., Fermigier, M., Stone, H. A. and Bibette, J. (2006). Microscopic artificial swimmers. *Nature*, 437, 862–865.
2. Bell, D. J., Leutenegger, S., Hammar, K. M., Dong, L. X. and Nelson, B. J. (2007). Three-dimensional control of engineered motile cellular microrobots. In *IEEE Int. Conf. Robotics and Automation (ICRA)*, Rome, Italy, pp. 1128–1133.
3. Ghosh, A. and Fischer, P. (2009). Controlled propulsion of artificial magnetic nanostructured propellers. *Nano Lett.*, 9, 2243–2245.

4. Behkam, B. and Sitti, M. (2007). Bacterial flagella-based propulsion and on/off motion control of microscale objects. *Appl. Phys. Lett.*, 90, 023902.
5. Magdanz, V., Sanchez, S. and Schmidt, O. G. (2013). Development of a sperm-flagella driven micro-bio-robot. *Adv. Mater.*, 25, 6581–6588.
6. Khalil, I. S. M., Dijkslag, H. C., Abelmann, L. and Misra, S. (2014). Magnetic propulsion of robotic sperms at low-Reynolds number. *Appl. Phys. Lett.*, 104, 223701.
7. Williams, B. J., Anand, S. V., Rajagopalan, J. and Saif, M. T. A. (2014). A self-propelled biohybrid swimmer at low Reynolds number. *Nature*, 5, 3081.
8. Berg, H. C. (1993). A self-propelled biohybrid swimmer at low Reynolds number. *Random Walks in Biology*, (Princeton University Press, Princeton, USA).
9. Purcell, E. M. (1977). Life at low Reynolds number. *Am. J. Phys.*, 45, 3–11.
10. Abbott, J. J., Peyer, K. E., Dong, L. and Nelson, B. (2009). How should microrobots swim? *The Int. J. Robot. Res.*, 28, 1434–1447.
11. Nelson, B. J., Kaliakatsos, I. K. and Abbott, J. J. (2010). Microrobots for minimally invasive medicine. *Ann. Rev. Biomed. Eng.*, 12, 55–85.
12. Ye, Z., Régnier, S. and Sitti, M. (2014). Rotating magnetic miniature swimming robots with multiple flexible flagella. *IEEE Trans. Robot.*, 30, 3–13.
13. H. K. D, Kim, P. S. S., Julius, A. A. and Kim, M. J. (2012). Three-dimensional control of engineered motile cellular microrobots. In *IEEE Int. Conf. Robotics and Automation, Minnesota*, USA, pp. 721–726.
14. Ou, Y., Kim, D. H., Kim, P., Kim, M. J. and Julius, A. A. (2012). Motion control of magnetized Tetrahymena pyriformis cells by a magnetic field with Model Predictive Control. *Int. J. Robot. Res.*, 31, 1–11.
15. Julius, A. A., Sakar, M. S., Steager, E., Cheang, U. K., Kim, M. J. and Pappas, K. V, G. J. (2009). Harnessing bacterial power in microscale actuation. In *IEEE Int. Conf. Robotics and Automation*, Kobe, Japan, pp. 1004–1009.
16. Martel, S., Tremblay, C. C., Ngakeng, S. and Langlois, G. (2006). Controlled manipulation and actuation of micro-objects with magnetotactic bacteria. *Appl. Phys. Lett.*, 89, 3904.
17. Khalil, I. S. M., Pichel, M. P. L. A. and Misra, S. (2013). Closed-loop control of magnetotactic bacteria. *Int. J. Robot. Res.*, 32, 637–649.
18. Hassan, H., Pichel, M., Hageman, T., Abelmann, L. and Khalil, I. S. M. (2016). Influence of the magnetic field on the two-dimensional control of magnetospirillum gryphiswaldense strain msr-1. In *Proc. IEEE/RSJ Int. Conf. Robotics and Systems (IROS)*, Daejeon, Korea, pp. 5119–5124.
19. Lu, Z. and Martel, S. (2006). Preliminary investigation of bio-carriers using magnetotactic bacteria. In *Proc. IEEE Engineering in Medicine and Biology Society Annual International Conference (EMBS)*, New York City, USA, pp. 683–686.
20. S. M. and Mohammadi, M. (2010). Using a swarm of self-propelled natural microrobots in the form of flagellated bacteria to perform complex micro-assembly tasks. In *IEEE Int. Conf. Robotics and Automation (ICRA)*, Alaska, USA, pp. 500–505.
21. Lu, Z. and Martel, S. (2007). Controlled bio-carriers based on magnetotactic bacteria. In *Proc. IEEE Int. Conf. Solid-State Sensors, Actuators and Microsystems*, Lyon, France, pp. 683–686.
22. Khalil, I. S. M., Magdanz, V., Sanchez, S., Schmidt, O. G. and Misra, S. (2014). Biocompatible, accurate, and fully autonomous: A sperm-driven micro-bio-robot. *J. Micro-Bio Robot.*, 9(3–4), 79–86.
23. Honda, T., Arai, K. I. and Ishiyama, K. (1996). Micro swimming mechanisms propelled by external magnetic fields. *IEEE Trans. Magnet.*, 32, 5085–5087.
24. Khalil, I. S. M., Pichel, M. P., Sukas, O. S., Abelmann, L. and Misra, S. (2013). Control of magnetotactic bacterium in a micro-fabricated maze. In *IEEE Int. Conf. Robotics and Automation*, Karlsruhe, Germany, pp. 5488–5493.

25. Pak, O. S. and Lauga, E. (2015). Chapter in Low-Reynolds-Number Flows: Fluid-Structure Interactions. In eds. Duprat C. and Stone, A. H. *Royal Soc. of Chemistry Soft Matter Series*, ISBN 978-1-84973-813-2.
26. Taylor, G. (1951). Analysis of the swimming of microscopic organisms. *Proc. Roy. Soc. Lond.*, 209, 447–461.
27. Khalil, I. S. M., Youakim, K., Sánchez, A. and Misra, S. (2014). Magnetic-based motion control of sperm-shaped microrobots using weak oscillating magnetic fields. In *Proc. IEEE Int. Conf. Robotics and Systems (IROS)*, Chicago, USA, pp. 4686–4691.
28. Khalil, I. S. M., Tabak, A. F., Hosney, A., Mohamed, A., Klingner, A., Ghoneima, M. and Sitti, M. (2016). Sperm-shaped magnetic microrobots: Fabrication using electrospinning, modeling, and characterization. In *IEEE Int. Conf. Robotics and Automation*, Stockholm, Sweden, pp. 1939–1944.
29. Kaneko, T. (1975). On Timoshenko's correction for shear in vibrating beams. *J. Phys. D: Appl. Phys.*, 8, 1927–1936.
30. Rosinger, H. E. and Ritchie, G. (1977). On Timoshenko's correction for shear in vibrating isotropic beams. *J. Phys. D: Appl. Phys.*, 10, 1461–1466.
31. Choi, H., Choi, J., Jang, G., oh Park, J. and Park, S. (2009). Two-dimensional locomotion of a microrobot with a novel stationary electromagnetic actuation system. *Smart Mater. Struct.*, 18, 055007–1–055007–9.
32. Jeon, S., Jang, G., Choi, H. and Park, S. (2010). Magnetic navigation system with gradient and uniform saddle coils for the wireless manipulation of micro-robots in human blood vessels. *IEEE Trans. Magnet.*, 46, 1943–1946.
33. Tabak, A. F. and Yesilyurt, S. (2014). Improved kinematic models for two-link helical micro/nanoswimmers. *IEEE Trans. Robot.*, 30, 14–25.
34. Brennen, C. and Winet, H. (1977). Fluid mechanics of propulsion by cilia and flagella. *Ann. Rev. Fluid Mech.*, 9, 339–398.
35. Beiranvand, R. (2013). Magnetic field uniformity of the practical tri-axial Helmholtz coils systems. *Rev. Sci. Instrum.*, 84, 075109–1–075109–11.
36. Kummer, M. P., Abbott, J. J., Kartochvil, B. E., Borer, R., Sengul, A. and Nelson, B. J. (2010). OctoMag: An Electromagnetic System for 5-DOF Wireless Micromanipulation. *IEEE Trans. Robot.*, 26, 1006–1017.
37. Peyer, K. E., Zhang, L. and Nelson, B. J. (2012). Bio-inspired magnetic swimming microrobots for biomedical applications. *Nanoscale*, 5, 1259–1272.
38. Li, D. and Xia, Y. (2004). Electrospinning of nanofibers: Reinventing the wheel? *Adv. Mater.*, 16, 1151–1170.
39. Khalil, I. S. M., Tabak, A. F., Klingner, A. and Sitti, M. (2016). Swimming in low Reynolds Numbers using planar and helical flagellar waves. *Appl. Phys. Lett.*, 109, 033701.
40. Paxton, W. F., Kistler, K. C., Olmeda, C. C., Sen, A., Angelo, S. K. S., Cao, Y., Mallouk, T. E., Lammert, P. E. and Crespi, V. H. (2004). Catalytic nanomotors: Autonomous movement of striped nanorods. *J. Am. Chem. Soc.*, 126, 13424–13431.
41. Calvo-Marzal, P., Sattayasamitsathit, S., Balasubramanian, S., Windmiller, J. R., Dao, C. and Wang, J. (2010). Propulsion of nanowire diodes. *Chem. Commun.*, 46, 1623–1624.
42. Wang, W., Li, S., Mair, L., Ahmed, S., Huang, T. J. and Mallouk, T. E. (2014). Acoustic Propulsion of Nanorod Motors Inside Living Cells. *Angewandte Chemie*, 126, 3265–3268.
43. Kratochvil, B. E., Kummer, M. P., Erni, S., Borer, R., Frutiger, D. R., Schrule, S. and Nelson, B. J. (2010). Minimag: A hemispherical electromagnetic system for 5-dof wireless micromanipulation. In *Proc. 12th Int. Symp. Experimental Robotics*, New Delhi, India.
44. Mahoney, A. W., Cowan, D. L., Miller, K. M. and Abbott, J. J. (2012). Control of untethered magnetically actuated tools using a rotating permanent magnet in any position. In *Proc. IEEE Int. Conf. Robotics and Automation (ICRA)*, Minnesota, USA, pp. 3375–3380.

45. Abbott, J. J., Ergeneman, O., Kummer, M. P., Hirt, A. M. and Nelson, B. J. (2007). Modeling magnetic torque and force for controlled manipulation of soft-magnetic bodies. *IEEE Trans. Robot. Autom.*, 23, 1247–1252.
46. Khalil, I. S. M., Magdanz, V., Sanchez, S., Schmidt, O. G. and Misra, S. (2013). Three-dimensional closed-loop control of self-propelled microjets. *Appl. Phys. Lett.*, 103, 172404.
47. Mahoney, A. W. and Abbott, J. J. (2012). Control of untethered magnetically actuated tools with localization uncertainty using a rotating permanent magnet. In *Proc. IEEE RAS/EMBS Int. Conf. Biomedical Robotics and Biomechatronics (BioRob)*, Rome, Italy, pp. 1632–1637.
48. Hosney, A., Klingner, A., Misra, S. and Khalil, I. S. M. (2015). Propulsion and steering of helical magnetic microrobots using two synchronized rotating dipole fields in three-dimensional space. In *Proc. IEEE/RSJ Int. Conf. Robotics and Systems (IROS)*, Hamburg, Germany, pp. 1988–1993.
49. Khalil, I. S. M., Tabak, A. F., Sadek, K., Mahdy, D., Hamdi, N. and Sitti, M. (2017). Rubbing against blood clots using helical robots: Modeling and *in vitro* experimental validation. *IEEE Robot. Autom. Lett.*, 2, 927–934.
50. Hosney, A., Abdalla, J., Amin, I. S., Hamdi, N. and Khalil, I. S. M. (2016). *In vitro* validation of clearing clogged vessels using microrobots. In *Proc. IEEE RAS/EMBS Int. Conf. Biomedical Robotics and Biomechatronics (BioRob)*, Singapore, pp. 272–277.
51. Mahoney, A. W., Nelson, N. D., Parsons, E. M. and Abbott, J. J. (2012). Non-ideal behaviors of magnetically driven screws in soft tissue. In *Proc. IEEE/RSJ Int. Conf. Robotics and Systems (IROS)*, Vilamoura, Portugal, pp. 3559–3564.
52. Nelson, N. D., Delacenserie, J. and Abbott, J. J. (2013). An empirical study of the role of magnetic, geometric, and tissue properties on the turning radius of magnetically driven screws. In *Proc. IEEE Int. Conf. Robotics and Automation (ICRA)*, Karlsruhe, Germany, pp. 5372–5377.
53. Servant, A., Qiu, F., Mazza, M., Kostarelos, K. and Nelson, B. J. (2015). Controlled in vivo swimming of a swarm of bacteria-like microrobotic flagella. *Advan. Mater.*, 27, 2981–2988.
54. Gabriel Stokes (1851). On the effect of the internal friction of fluids on the motion of pendulums. *Transactions of the Cambridge Philosophical Society*, 9, 8–106.
55. Osborne Reynolds (1883). An experimental investigation of the circumstances which determine whether the motion of water shall be direct or sinuous, and of the law of resistance in parallel channels. *Philosophical Transactions of the Royal Society*, 174(0), 935–982.